COMPUTATIONAL CONTINUUM MECHANICS

ВЫЧИСЛИТЕЛЬНАЯ МЕХАНИКА СПЛОШНЫХ СРЕД

Computational Continuum Mechanics. 2022. Vol. 15. No. 2. pp. 234-246 DOI: 10.7242/1999-6691/2022.15.2.18

MODELING OF AMg6 ALLOY RECRYSTALLIZATION IN THE FORGED LAYER DURING THE OVERLAY WELDING OF A MATERIAL IN THE PROCESS OF HYBRID ADDITIVE MANUFACTURING

N.K. Salikhova[1,2], D.S. Dudin[1,2], I.E. Keller[1,2], A.A. Oskolkov[2], A.V. Kazantsev[2] and D.N. Trushnikov[2]

[1]*Institute of Continuous Media Mechanics UB RAS, Perm, Russian Federation*
[2]*Perm National Research Polytechnic University, Perm, Russian Federation*

The paper deals with static recrystallization during the metal layer welding over the face of a prismatic specimen pre-treated with plastic deformation. The study aims at solving the problem of selecting rational parameters for hybrid additive manufacturing of light and high-strength linear elements of segmented structures made of aluminum-magnesium alloys using the layer-by-layer forging with a pneumatic hammer. For this purpose, the two independent problems of the one-sided forging of a prismatic specimen and temperature evolution during the plasma-arc welding of a layer over the same specimen are solved numerically. The fields of accumulated deformations and the history of temperature changes in the specimen are used to calculate the volume fraction of the statically recrystallized material in the work-hardened layer under thermal cycle temperature. The calculations of forging were performed based on the LS-DYNA® package, the thermal problem was solved in Comsol Multiphysics®, and the fraction of the recrystallized material was calculated by making use of the Wolfram Mathematica system. In the numerical model, the impact of the pneumatic hammer was estimated by means of a strain-gauged steel target, and then it was verified by evaluating the distortions of the cross-section of the forged bar made of AMg6 alloy measured in the experiment. The thermal effect is calculated taking into account the PI controller, which automatically controls the overlaying process in the hybrid additive manufacturing plant. The volume fraction of a statically recrystallized material was calculated using Avrami's law and data on the dependence of the time of 50 % transformation of the material on the accumulated deformation and the temperature taken from the literature about aluminum-magnesium alloy 5083, which is similar to AMg6. The model predicts a high sensitivity of the fraction of the recrystallized material to a previous plastic deformation and to the maximum temperature in the thermal cycle of the overlay welding, so it results in a more localized boundary layer of the recrystallized material compared to the boundary layer under plastic deformation. The calculation results demonstrate effectiveness of the layer-by-layer pressure shaping strategies aimed at providing deep-layer plastic deformation. In terms of the degree of recrystallization, the use of rational modes of the overlay welding and forging ensure the synthesis of products with high strength and ductility characteristics during hybrid additive manufacturing.

Key words: additive manufacturing, layer-by-layer forging, static recrystallization, aluminum-magnesium alloys, numerical calculation, experimental confirmation

1. Research problem and aims

Wire-arc additive manufacturing creates light and strong metal structures of complex shapes with significant material savings. In order to achieve strength and resource characteristics similar to a rolled metal, effective plasma weld overlay (WOL) technologies (including consumable electrode), cold metal transfer, subsequent heat treatment are developed, and optimal process modes are selected [1]. The strength and ductility of metal alloys produced in this case are limited by the dendritic structure of the crystallites. The formation of such a microstructure can be suppressed using hybrid additive manufacturing, in which the overlay of a linear element of a segmented structure is forged with a pneumatic tool (pneumatic hammer) or rolled. Such technologies have been developed in the last ten years in a number of research organizations: Cranfield and Manchester Universities [2–5], Indian Institute of Technology Bombay [6, 7], Perm National Research Polytechnic University [8–11], Bryansk State Technical University [12, 13].

There are various theories for the formation of a homogeneous fine-grained structure in a metal during hybrid additive manufacturing. Such a microstructure is gained due to solid-state transformations during recrystallization (in aluminum-magnesium alloys) or phase transformations (in titanium alloys and stainless steels) occurring in a work-hardened metal under thermal cycle conditions during WOL. The layer-by-layer forging also suppresses surface dendrite nucleations by replacing the surface grain nucleation mechanism with a bulk one.

Email addresses for correspondence: salikhova@icmm.ru

This work is aimed at studying the recrystallization in a hybrid additively manufactured material from aluminum-magnesium alloy AMg6. According to the maps of plastic deformation mechanisms, this process observes the static recrystallization in the near-surface layer of a solid material, which depends on the accumulated plastic deformation acquired during forging and occurs during heating of the next overlay. Since the processes of plastic deformation and heating take place sequentially, in the first approximation they are considered unrelated. The corresponding problems are solved numerically in a separate way using the LS-DYNA® and Comsol Multiphysics® packages. Then, according to the field of the accumulated plastic deformation determined as a result of solving these problems and the history of temperature distributions in the specimen, the field of the volume fraction of the recrystallized material is calculated using the Avrami law in the Wolfram Mathematica package. To supplement the numerical model with the impact characteristics of the pneumatic hammer, equivalent to the real ones, a strain-gauged steel target was used, as well as the data on the distortion of the cross-section of a single forged specimen. The plastic properties of AMg6 in a wide range of strain rates were determined from the necessary static and dynamic tests using the Hopkinson–Kolsky method. The Avrami's law data for Alloy 5083, similar to AMg6, for the required values of the accumulated strain and temperature were taken from the literature.

The calculated spatial distribution of the volume fraction of the recrystallized material, depending on the degree of forging, can serve as a tool aimed at choosing its correct parameters when obtaining products with high ductility and strength characteristics based on hybrid additive technologies.

2. Finding impact characteristics during forging

A model problem of one-sided forging of a straight prismatic elastic-plastic bar, the opposite face of which was rigidly fixed on a massive plate, was considered for a numerical study of the evolution patterns of the spatial distribution of the volume fraction of recrystallized material. Uniform forging along a linear specimen was carried out. This method refers to the "point" technologies of pressure treatment, accompanied by the localization of plastic deformation near the treated surface.

To find the characteristics of the impact force of the pneumatic hammer, the following experiment was carried out: a specimen bar sized 150×23.7×10.3 mm was cut from rolled AMg6 products and annealed for 3 hours at 550°C with subsequent cooling in air, then it was rigidly and uniformly fixed with five screws on a steel plate pressed against the working surface of an automatic hybrid additive manufacturing plant, designed on the basis of a metalworking center (Fig. 1*a*). The specimen was forged with an SA7401H AIRPRO pneumatic hammer attached to the plant pillar. For effective forging of the overlay segment, we used a cylindrical striker with a spherical tip of 15 mm radius (Fig. 1*b*). Optimal parameters were preliminarily determined experimentally: the working pressure was 0.6 MPa, the striker pressure was 0.2 MPa, and feed rate was $v = 300$ mm/min, which provided a uniform hammering of the linear element.

The analysis of signals from a strain-gauged steel target, which is a hundred-millimeter piece of railway rail P24 (Fig. 2*a*). Data from two strain gauges installed vertically on both sides of the rail neck were fed to the strain gauge station ZET 017-U4. Deformation $\varepsilon(t)$, filtered from high frequency acoustic noise, made it possible to reconstruct the equivalent force of the tool $F(t) = F_0\left(4/3 + \sin 2\pi t/\nu\right)$, $F_0 = 10$ kN, $\nu = 47$ Hz, which caused similar deformations of the rail neck at the control point (see Fig. 2*b*). To do this, the

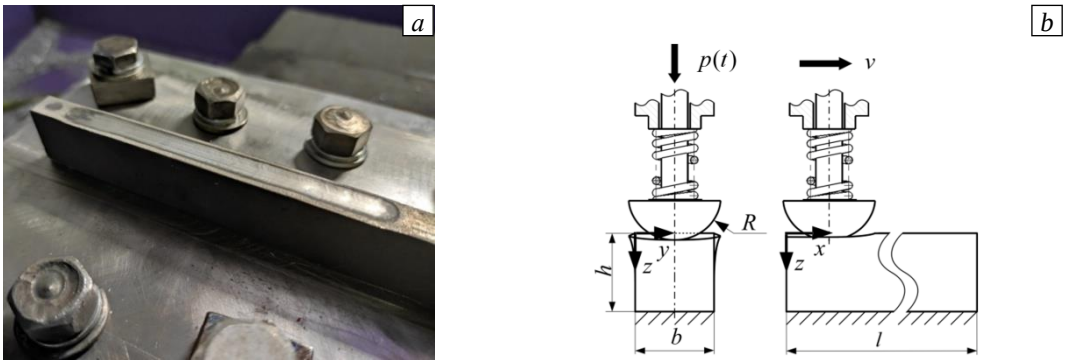

Fig. 1. Control specimen forged with a pneumatic hammer, (*a*) and the forging process scheme (*b*).

corresponding elastoplastic problem was solved in the LS-DYNA® package. The work of plastic

deformation in one stroke of the striker corresponded to an impact energy of 20 J, which was specified in the passport of the tool.

Thin transverse layers were cut from the control specimen, forged from the narrow side, on the electroerosive machine, the plane-parallel faces of which were polished. The specimen cross-sectional distortion (Fig. 3*a*), measured using a Hirox KH-7700 digital optical microscope, was localized at a depth with a half-maximum of 5.0 mm from the forging surface with a hole 9.3 mm wide and 0.8 mm deep. This distortion was reproduced in the numerical calculation of the AMg6 specimen forging [14] with the parameters of impact of the pneumatic hammer which ensured their independent confirmation.

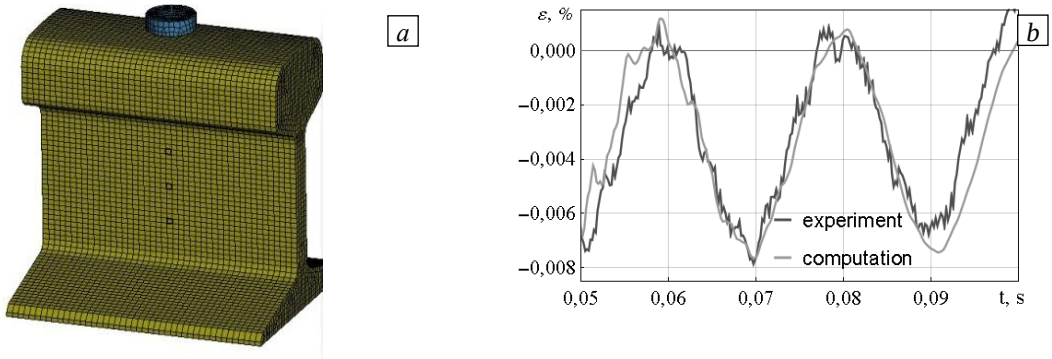

Fig. 2. Computational scheme for forging a target (rail) (*a*) and deformation of its neck at the control point (in the middle of the three shown) (*b*). На рисунке кириллица: эксперт, расчет

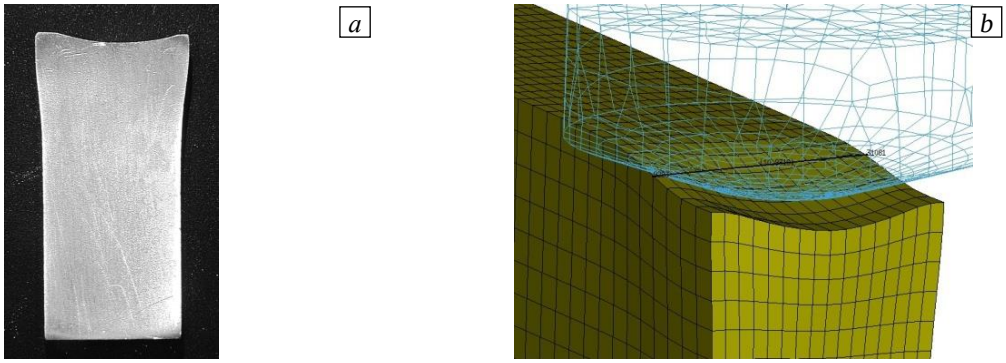

Fig. 3. Distorted cross-section of the AMg6 specimen (*a*) and its reproduction in numerical calculation (*b*).

3. Elastic-plasticity model of a material and its identification

To describe large plastic and small elastic deformations of metals, the standard model [15, 16] was used in terms of the current Lagrangian approach in rates, numerically implemented in the LS-DYNA® package. The additivity of the elastic and plastic tensors of the strain rates is accepted, while the elastic tensor is linearly related to the Jaumann derivative of the Kirchhoff stress tensor, and the plastic tensor $\dot{\varepsilon}_{ij}^{p}$ with the Cauchy stress tensor σ_{ij} by means of the plastic flow law of:

$$\dot{\varepsilon}_{ij}^{p} = \dot{\lambda}\frac{\partial \phi}{\partial \sigma_{ij}},$$

where $\phi = \phi_M$ is the plastic potential associated with the von Mises yield criterion

$$\phi_M = \frac{\sigma_i^2}{\sigma_u^2} - 1 = 0.$$

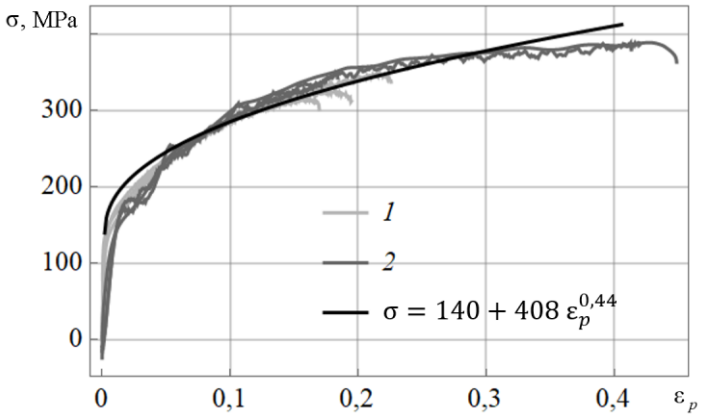

Fig. 4. Deformation curves of AMg6 at loading rates of $3\cdot10^{-4}$ s^{-1} (*1*) and $2\cdot10^{3}$ s^{-1} (*2*) in the coordinates of true stresses and logarithmic strains, as well as their approximation.

Here $\sigma_i = \sqrt{3s_{ij}s_{ij}/2}$ is the intensity of stresses, $s_{ij} = \sigma_{ij} - \sigma_m\delta_{ij}$ are the components of the stress deviator, $\sigma_m = \sigma_{kk}/3$ is the mean stress; σ_u is the uniaxial tensile yield strength, for which the Johnson–Cook isotropic hardening law is adopted in the following form:

$$\sigma_u = \left(A + B\varepsilon_p^n\right)\left(1 + C\ln\frac{\dot{\varepsilon}_p}{\dot{\varepsilon}_*}\right),$$

where $\dot{\varepsilon}_p = \sqrt{2\dot{\varepsilon}_{ij}^p\dot{\varepsilon}_{ij}^p/3}$ is the intensity of plastic strain rates, $\varepsilon_p = \int_0^t \dot{\varepsilon}_p dt$ are the accumulated plastic deformations.

In the calculations, the density and Poisson's ratio were taken equal to $\rho_0 = 2640$ kg/m^3, and $\nu = 0.3$. Johnson–Cook hardening law constants $A = 140$ MPa, $B = 408$ MPa, $C = 0$, $\dot{\varepsilon}_* = 1$, $n = 0.44$ and the elastic modulus $E = 71$ GPa for AMg6 were found experimentally. To do this, quasi-static tensile tests were carried out with the strain rate of $3\cdot10^{-4}$ s^{-1} at room temperature using a Shimadzu AG-Xplus Electromechanical Universal Testing Machine. Three flat specimens of blades No. 23 (according to GOST 1497-84) were cut out from the annealed sheet metal on the electroerosive machine. During the tests, we used a video extensometer to record the longitudinal relative movement of the marks on the working part of the specimen and the relative narrowing of the working part of the specimen, along which the true stresses were then found. Dynamic compression tests of cylindrical specimens were performed by the Kolsky method [17, 18] on a split Hopkinson rod. The tests were carried out at room temperature and strain rates from 200 to 2000 s^{-1}. Figure 4 shows experimental strain curves in true stresses and strains. Dynamic curves are within the statistical error of quasi-static curves; therefore, the approximation by the Johnson–Cook law does not contain a rate factor, while taking into account the range from the yield stress to the limit of uniform elongation.

In the numerical solution of the contact dynamic problem by the finite element method, an 8-node parallelepiped with a single integration point was used to approximate the computational domain. The domain consisted of 90×16×16 elementary parallelepipeds with length $l_x = 1.67$ mm, width $l_y = 1.64$ mm and height $l_z = 1.48$ mm. A correct transition to a discrete analogue in the contact nodes and on the faces of the elements was achieved by selecting the contact stiffness coefficient. The coefficient of dry friction was assumed to be zero. To regularize the problem, in accordance with the recommendations of the software developers [19], acceptable coefficients of dissipation of the kinetic energy of the system were selected. Rayleigh dissipation coefficient $\beta = 0.1$ s provided filtering of acoustic components and computational speed.

The characteristics of the boundary layer profile of the accumulated plastic deformations near the forging plane (maximum value $\varepsilon_p = 0.2$ and half-maximum depth $z_{05}^{\varepsilon} = 5$ mm) for the AMg6 specimen under consideration with a single pass of the tool were obtained earlier in [14]. For a more complete

recrystallization of the material, higher values of these characteristics were required. They were achieved with double or triple passes of the tool. For such regimes, numerical calculations gave the following values: $\varepsilon_p = 0.4$, $z_{05}^{\varepsilon} = 6$ mm (for double forging) and $\varepsilon_p = 0.48$, $z_{05}^{\varepsilon} = 6.5$ mm (for triple forging).

4. Solving the problem of heat conductivity

The non-stationary problem of heat conductivity in a rectangular parallelepiped was solved (a bar specimen), one side of which had an overlay (Fig. 5*a*). In the hybrid additive manufacturing plant, the automatic control of the heat supply power with the plasma torch is implemented to ensure the uniformity of the process [20]. This makes it possible to deposit a layer of a constant l_z and set the finite element mesh to a single size along the normal coordinate. The WOL rate was $v_x = 1$ mm/s, the feeding of wire with a diameter of 1.2 mm and the rate of 13.5 mm/s. The following algorithm was implemented to simulate thermal processes during WOL. A layer of space of thickness l_z above the deposition edge was broken into tetrahedral finite elements (Fig. 5*b*). The presence of the heat source and the change in thermophysical constants in the domain of the weld pool were set using a moving indicator function:

$$I(x,y,z,t) = \left(h(z+l_z) - h(z)\right)\left(h(y) - h(y-16l_y)\right)\left(h(x-v_x t) - h(x-v_x t-6l_x)\right),$$

where $h(s) = \{0,\ s<0;\ 1,\ s\geq 0\}$ is Heaviside function, $\int_{-\infty}^{\infty}\int_{-\infty}^{\infty}\int_{-\infty}^{\infty} I(x,y,z,t)\,dxdydz = 6l_x \cdot 16l_y \cdot l_z = V_*$.

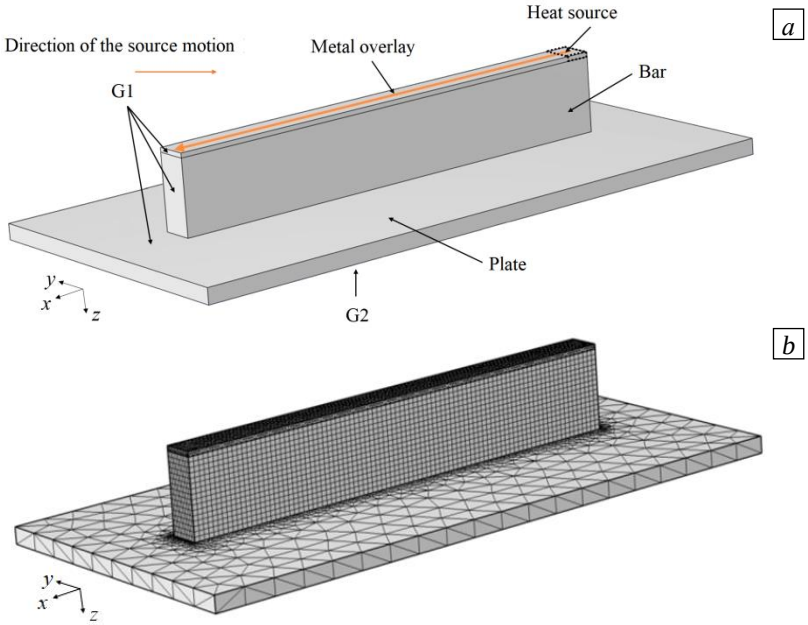

Fig. 5. Computational scheme of the metal WOL on the face of the bar (*a*) and split of the computational domain into finite elements (*b*).

In the computational domain, the heat conduction equation was solved:

$$\rho c_p \frac{\partial T}{\partial t} = \nabla \cdot (\lambda \nabla T) + q,$$

where T is the absolute temperature, ρ is the material density, c_p and λ coefficients of specific thermal capacity and conductivity, ∇ is Hamiltonian operator, q is the specific capacity of the heat source.

On the surface G1 of the entire computational domain (except for the lower face of the plate G2), the conditions for radiative and convective heat exchanges with the environmental medium were set:

$$-\lambda \mathbf{n} \cdot \nabla T = \varepsilon_T \sigma_{SB} \left(T^4 - T_0^4 \right) + k \left(T - T_0 \right).$$

Here k is the heat transfer coefficient from the surface to the environment; T_0 is the absolute temperature of the environment; σ_{SB} is the Stefan-Boltzmann constant; ε_T is the thermal emissivity; $\mathbf{n}$ is the external normal vector to the boundary. The surface G2 of the plate was considered thermally insulated: $\lambda \mathbf{n} \cdot \nabla T = 0$. Internal interfaces, i.e. melting and crystallization fronts were not considered in the model. Homogeneous initial conditions were set for the entire computational domain: $T\left(t = 0\right) \equiv T_0$.

The volumetric heat source in the form of a rectangular parallelepiped with the size $6l_x \times 16l_y \times l_z$ and volume V_* moved with the speed v_x along x axis, thus, the overlay was added to the computational domain. In the Comsol Multiphysics® package, the heat conduction problem was solved using an implicit integration scheme, with a time step of 0.1 s. The heat source power in a given volume V_* was computed according to formula $P(t) = \int_{-\infty}^{\infty} \int_{-\infty}^{\infty} \int_{-\infty}^{\infty} q(x,y,z,t)\,dxdydz = V_* q_*(t)$, where $q(x,y,z,t) = I(x,y,z,t) q_*(t)$, and, as mentioned above, it was automatically adjusted for the uniformity of heating during the WOL. The volume of the weld pool, having a depth greater than the thickness of the deposited metal layer l_z by the depth of the penetration zone of the bar specimen ($z_S > l_z$) was determined based on the solidus temperature: $T(V_S) \geq T_S$. The WOL process at each time step was controlled by the discrepancy $u(t) = \left(V_S(t) - V_{**}\right)/V_{**}$ with a position-integrating controller:

$$P(t+\tau) = P(t) - K_p P(t) u(t) - K_I P(t) \int_0^t u(t)\,dt, \qquad P(0) = P_0.$$

While V_{**} was the set value of the pool volume and was 1.25 volume of the heat source V_* at a penetration depth of the bar up to 1 mm; K_p, K_I are the coefficients of the positional and integrating links of the controller, were selected from the stability conditions and process quality criteria.

It was assumed that the specific power of the heat source $q_*(t) = P(t)/P(t)$ was homogeneously distributed in volume V_* at the current time. Simultaneously with the heat source in the WOL region, the density and thermophysical characteristics of the material were set, as well as the conditions on the added outer boundary G1. A macro has been written in Comsol Multiphysics® to implement the algorithm. The values of thermophysical and other constants of the model adopted in the calculation are summarized in Table 1.

Table 1. Constants adopted in the heat conduction model.

Constants	Symbol	Unit measure	Value
Solidus temperature of AMg6	T_S	°C	550
Ambient temperature	T_0	°C	20
Specific heat capacity of AMg6	c_p	$J \cdot kg^{-1} \cdot K^{-1}$	922
Mass density of AMg6	ρ	$kg \cdot m^{-3}$	2640
Thermal conductivity coefficient of AMg6	λ	$W \cdot m^{-1} \cdot K^{-1}$	122
Thermal radiation coefficient of AMg6	ε_T	–	0.33
Heat transfer coefficient of AMg6 in air	k	$W \cdot m^{-2} \cdot K^{-1}$	15
Stefan-Boltzmann constant	σ_{SB}	$W \cdot m^{-2} \cdot K^{-2}$	$5.67 \cdot 10^{-8}$
Initial heat source power	P_0	W	800

Position link coefficient	K_p	–	0.8
Integrating factor	K_I	s^{-1}	0.005

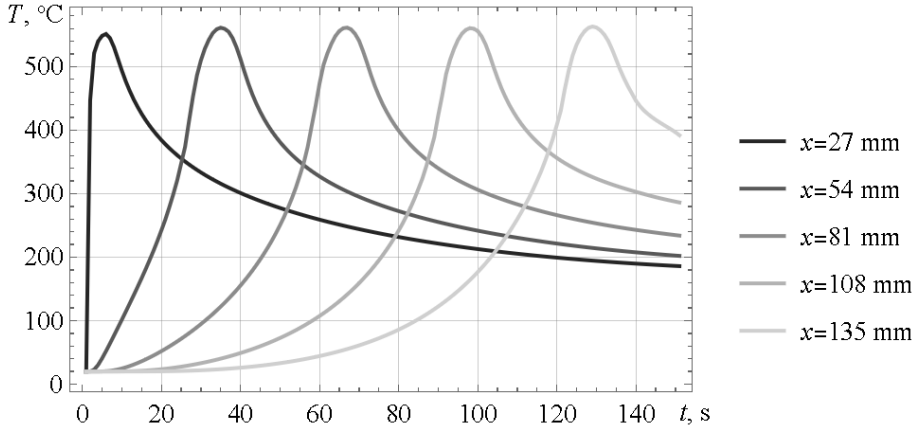

Fig. 6. Evolution of the longitudinal temperature profile in the upper layer of finite elements at different positions of the heat source during WOL.

Figure 6 shows the results of modeling the distribution of the temperature profile in the longitudinal plane of symmetry of the specimen for the upper layer of finite elements located under the overlay, directly in contact with it, at different positions of the heat source during one WOL. The results show the stability of the maximum temperature and its profile near the maximum point, which plays an important role in the recrystallization process.

5. Model of static recrystallization and its identification

Various models are used to calculate the recrystallization of grains or phase transformations under thermomechanical loading, which accompanies the pressure treatment of metal alloys. The possibility of correct determining the material constants from experimental data is provided primarily by phenomenological models with a minimum number of microstructural variables and factors that control changes in the microstructure. To describe the static recrystallization of the forged metal during the deposition cycle, models are used with one microstructural parameter, which is the proportion of the transformed material depending on the accumulated plastic deformations and the history of temperature changes. According to [21], this type of transformation is diffusion-controlled. In the near-boundary forged layer, which is characterized by a depth of half-maximum of the accumulated plastic deformations of 5–7 mm and their maximum values of 0.2–0.5 (with a single to triple tool passes), a high density of dislocations takes place. During the WOL cycle, this layer is melted to a depth of up to 1 mm, and new equiaxial grains appear in the remaining solid material in the zones with high dislocation density.

The Avrami (Johnson–Mel–Avrami–Kolmogorov) model is the most widely used to describe the static recrystallization [21–28]:

$$f = 1 - \exp\left(-\beta \left(\frac{t}{t_{05}} \right)^n \right), \tag{1}$$

where f is the volume fraction of the transformed material, t_{05} is the time it takes for half of the material to be transformed, $\beta = \ln 2$. As a rule, it is assumed that $t_{05} = g(\varepsilon_p, T)$, $g(\varepsilon_p, T) = \zeta \varepsilon_p^m \exp(Q/RT)$ and $n = h(T)$. Expression (1) is the solution of Equation:

$$\dot{f} = \alpha t^{n-1} (1 - f), \tag{2}$$

which is more convenient to use in conditions of changing temperatures; here $\alpha = n\ln 2/t_{05}^{n}$. If the experiments at the constant temperature and accumulated plastic deformation determine the function $t_*\left(T,\varepsilon_p\right)$ which is the time during which the proportion of the converted material reaches value $f_* < 1$, then the computation of recrystallization in non-isothermal processes can be performed using the summation principle [21]:

$$f = f_* \int_0^t \frac{dt}{t_*\left(T(t),\varepsilon_p\right)}. \tag{3}$$

The Leblond–Deveaux model is also used [29]:

$$\dot{f} = g\left(\dot{T}\right)\frac{f_{eq}(T) - f}{t_*\left(T,\varepsilon_p\right)}, \tag{4}$$

where $f_{eq}(T)$ is the equilibrium volume fraction which clearly distinguishes function $g\left(\dot{T}\right)$ and considers the cooling rate.

To determine the material constants of the Avrami law (1) for the AMg6 alloy, we used the experimental data [30] for the 5083 alloy with a similar chemical composition, which were approximated again here. As a result, we obtained the following:

$$t_{05} = 2.2\cdot 10^{-14}\left(1+\frac{4.3}{\varepsilon_p^3}\right)\exp\left(\frac{1.9\cdot 10^5}{RT}\right), \quad n = 0.81. \tag{5}$$

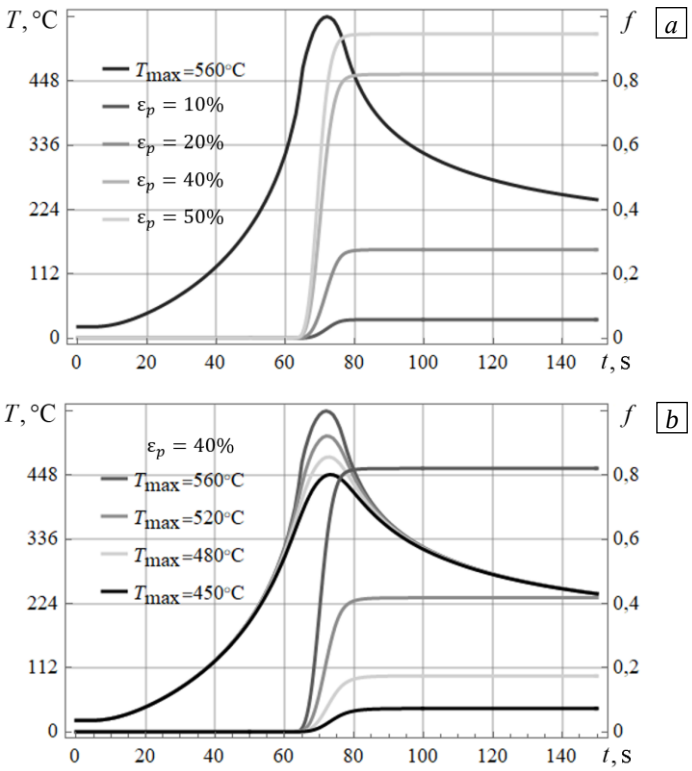

Fig. 7. Evolution of the volume fraction of the recrystallized material during the thermal cycle depending on the preliminary accumulated plastic deformation (*a*) and the maximum temperature in the cycle (*b*).

Figure 7*a* shows the growth curves of the volume fraction of the recrystallized material depending on the amount of preliminary plastic deformation during the thermal cycle. As the latter, we took the history of temperature change found above at a point located at a depth of 1.3 mm in the longitudinal plane of symmetry of the specimen. The results demonstrate the sensitivity of the process to pre-deformation in the boundary layer of the forged specimen. With an increase in pre-strain, there is a noticeable increase in the growth rate of the fraction of the recrystallized material. It can also be seen that the process mainly develops in the high temperature range, which starts from a certain value depending on the preliminary deformation. For this, Figure 7*b* shows the dependence of the proportion of the recrystallized material on the maximum temperature in the thermal cycle at preliminary deformation of 0.4. Such nonlinearity contributes to a stronger localization in depth of the fraction of the recrystallized material in comparison with the accumulated plastic deformations.

6. The results of calculating the proportion of recrystallized material and comparison with the experiment

The solid-state transformation of the material in the specimen was calculated in the Wolfram Mathematica package according to Equation (2) with constants (5) from the accumulated plastic deformations and the history of temperature changes calculated at the previous stages.

Fig.8. demonstrates distributions over the cross-section of the specimen of the accumulated plastic deformation and the volume fraction of the recrystallized material due to temperature when depositing the layer on surface $z = 0$. Figure 8*b* shows that the layer of the recrystallized material is localized near the growing surface and its fraction is significantly lower near the sides of the specimen due to an insufficient degree of forging of these areas with a striker with a spherical tip (Fig. 8*a*). The profiles of the boundary layers of the proportion of the recrystallized material and the accumulated plastic deformation along the depth of the cross-section along the plane of symmetry for single, double and triple forging are shown in Figure 9. The narrower localization of the boundary layer of the proportion of the recrystallized material is noteworthy compared to the boundary layer of the accumulated plastic deformation, which has been predicted qualitatively above. With single forging, the ratio of the depths of the half-maxima of these values $z_{05}^{\varepsilon} / z_{05}^{f}$ is approximately equal to 2, with triple forging it is equal to 4. In addition, the maximum value of the volume fraction of the recrystallized material increases from 0.3 for single forging to 0.9 for double and triple forging. Approximately in the same proportion, the integral value of the volume of the recrystallized material also increases. With single forging, the depth of the half-maximum of the fraction of the recrystallized material is approximately 1 mm, with triple forging, it is 2 mm.

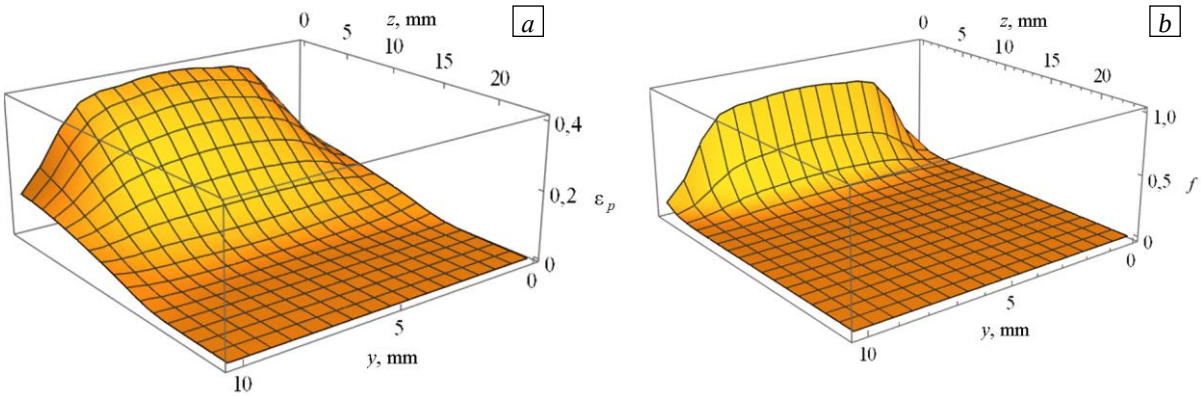

Fig. 8. Distribution over the cross-section of the specimen of the accumulated plastic deformation (*a*) and the volume fraction of recrystallized material (*b*) during double forging.

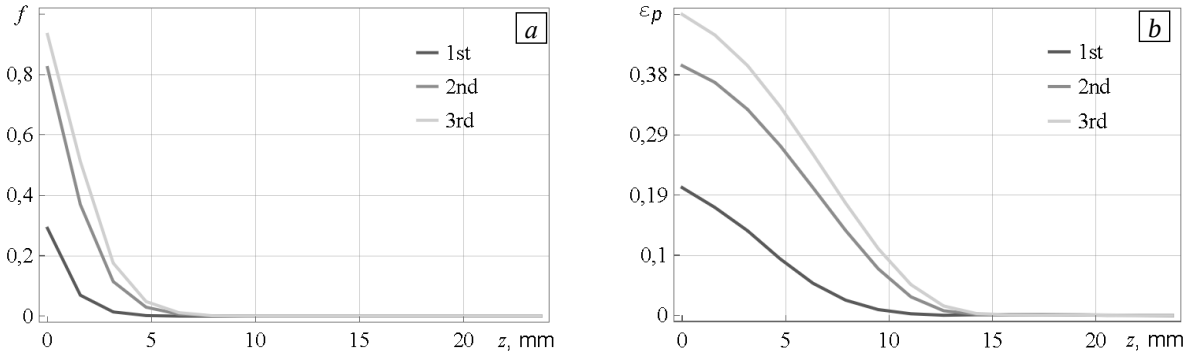

Fig. 9. Depth distribution of the volume fraction of recrystallized material (*a*) and accumulated plastic deformation (*b*) during single, double and triple forging.

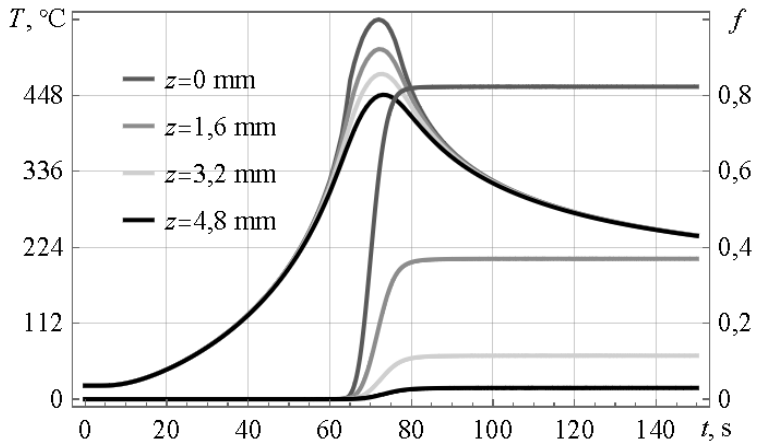

Fig. 10. Evolution of temperature and volume fraction of the recrystallized material depending on the distance from the surface of the deposition.

Figure 10 contains another presentation of the calculation results, i.e. for points located at different depths relative to the surface being built, the curves of temperature evolution and the growth of the proportion of the recrystallized material during the deposition are shown. These data show the sensitivity of the transformation process to the amount of the accumulated plastic deformation and the maximum temperature of the thermal cycle, which is described by the Avrami's law (Fig. 7).

An analysis of the calculated data allows us to conclude that with single forging of a linear segment, the characteristics of the boundary layer of the accumulated plastic deformation are not achieved, which are sufficient for complete static recrystallization of the material at a depth that reliably exceeds the depth of the weld pool during subsequent layer deposition. For more complete recrystallization of the material being grown, it is advisable to use such forging strategies that provide a greater thickness of the forged layer (or, in particular, the deeper occurrence of the point corresponding to the half-maximum of the distribution of the accumulated plastic deformation). This requires 2–3 pass-forging with pneumatic tools in the automatic hybrid additive manufacturing plant.

To study the effectiveness of the hybrid additive manufacturing technology with forging, tensile tests were performed according to [31]. These tests determined σ_B the temporary resistance, and δ the relative elongation after rupture were determined. We produced three standard specimens, such as blades, which were tested for tension at a speed movable grip 1 mm/min from the material manufactured using the technology of cold metal transfer from wire 5356 ESAB with a diameter of 1.2 mm with a zigzag deposition, without the use of layer-by-layer forging, as well as with single and triple layer-by-layer forging. For comparison, specimens from annealed rolled products AMg5 were also tested for tension. The test results summarized in Table 2 show that the triple layer-by-layer forging noticeably increases the strength and ductility characteristics of the material, and the single forging improves them slightly.

Table 2. Standard characteristics of strength and ductility of the studied materials

Characteristics / Method of manufacturing materials	σ_B, MPa	δ, %
Forging (annealed AMg5)	286±6	22±2
Additive manufacturing without layer forging	261±3	26±2
Additive manufacturing with single layer forging	265±5	27±2
Additive manufacturing with triple forging	278±5	36±6

7. Conclusions

The process of static recrystallization of an aluminum-magnesium alloy AMg6 during the thermal cycle of depositing the material layer on the face of a linear specimen, previously forged with a pneumatic tool, was numerically studied. The material with fine recrystallized grains has increased strength and ductility compared to the material deposited using additive technologies without layer-by-layer forging, which has a dendritic structure. For recrystallization of the material during the thermal cycle, work hardening is required, which in this case is created by forging the workpiece.

A detailed consideration of hybrid additive manufacturing during the material deposition on the surface made it possible to formulate the uncoupled model of the successive stages of forging, deposition and solid-state transformation of the material, depending on the accumulated plastic deformations and the history of temperature changes calculated in the previous stages. Each of the problems was solved numerically in the software package LS-DYNA®, Comsol Multiphysics® and Wolfram Mathematica with the identification of the necessary characteristics from the experimental data.

It has been established that for the AMg6 alloy, due to the significant nonlinearity of the law of static recrystallization (2), (5), in terms of accumulated plastic deformations and temperature, the layer of the synthesized material is localized with a characteristic depth, which is 2–4 times less than the characteristic depth of the accumulated plastic deformations at 1– 3 forging passes, respectively, which is 1–2 mm. Taking into account the partial penetration of the workpiece to a depth of 1 mm and the thickness of the deposited layer of about 1.5 mm, in order to obtain a material with the significant proportion of fine grains, it is recommended to use the double or triple forging of each deposited layer of the material during hybrid additive manufacturing. This recommendation has been experimentally confirmed.

The authors are grateful to their colleagues from the IMSS Ural Branch of the Russian Academy of Sciences Yu.V. Bayandin, M.V. Bannikov and V.V. Chudinov for testing and obtaining the constants of the hardening law AMg6, as well as E.S. Lobov for the experimental calibration of the impact of the pneumatic tool.

This work was supported by the Russian Science Foundation (Project No. 21-19-00715).

References

1. Wu B., Pan Z., Ding D., Cuiuri D., Li H., Xu J., Norrish J. A review of the wire arc additive manufacturing of metals: Properties, defects and quality improvement. *J. Manuf. Process.*, 2018, vol. 35, pp. 127-139. https://doi.org/10.1016/j.jmapro.2018.08.001
2. Colegrove P.A., Coules H.E., Fairman J., Martina F., Kashoob T., Mamash H., Cozzolino L.D. Microstructure and residual stress improvement in wire and arc additively manufactured parts through high-pressure rolling. *J. Mater. Process. Tech.*, 2013, vol. 213, pp. 1782-1791. https://doi.org/10.1016/j.jmatprotec.2013.04.012
3. Gu J., Wang X., Bai J., Ding J., Williams S.W., Zhai Y., Liu K. Deformation microstructures and strengthening mechanisms for the wire+ arc additively manufactured Al-Mg4.5Mn Alloy with inter-layer rolling. *Mater. Sci. Eng.*, 2018, vol. 712, pp. 292-301. https://doi.org/10.1016/j.msea.2017.11.113
4. Honnige J.R., Colegrove P.A., Ganguly S., Eimer E., Kabra S., Williams S. Control of residual stress and distortion in aluminium wire+arc additive manufacture with rolling. *Addit. Manuf.*, 2018, vol. 22, pp. 775-783. https://doi.org/10.1016/j.addma.2018.06.015
5. McAndrew A.R., Rosales M.A., Colegrove P.A., Hönnige J.R., Ho A., Fayolle R., Eyitayo K., Stan I., Sukrongpang P., Crochemore A., Pinter Z. Interpass rolling of Ti-6Al-4V wire+arc additively

manufactured features for microstructural refinement. *Addit. Manuf.*, 2018, vol. 21, pp. 340-349. https://doi.org/10.1016/j.addma.2018.03.006

6. Karunakaran K.P., Kapil S., Negi S. Multi-station multi-axis hybrid layered manufacturing system. Indian Patent. 2018. Application Number 201821038516.
7. Karunakaran K.P., Kapil S., Kulkarni P. In-situ stress relieving process for additive manufacturing. Indian Patent. 2016. Application Number 201621028306.
8. Shchitsyn Yu.D., Krivonosova E.A., Trushnikov D.N., Ol'shanskaya T.V., Kartashov M.F., Neulybin S.D. Use of CMT-surfacing for additive formation of titanium alloy workpieces. *Metallurgist*, 2020, vol. 64, pp. 67-74. https://doi.org/10.1007/s11015-020-00967-0
9. Shchitsyn Yu.D., Krivonosova E.A., Olshanskaya T.V., Neulybin S.D. Vliyaniye additivnoy plazmennoy naplavki na strukturu i svoystva splava sistemy alyuminiy – magniy – skandiy [Structure and properties of aluminium magnesium scandium alloy resultant from the application of plasma welding with by-layer deformation hardening]. *Tsvetnye metally – Non-ferrous Metals Journal*, 2020, no. 2, pp. 89-94. https://doi.org/10.17580/tsm.2020.02.12
10. Shchitsyn Y., Kartashev M., Krivonosova E., Olshanskaya T., Trushnikov D. Formation of structure and properties of two-phase Ti-6Al-4V alloy during cold metal transfer additive deposition with interpass forging. *Materials*, 2021, vol. 14, 4415. https://doi.org/10.3390/ma14164415
11. Trushnikov D.N., Kartashev M.F., Olshanskaya T.V., Mindibaev M.R., Shchitsyn Y.D., Saucedo-Zendejo F.R. Improving VT6 titanium-alloy components produced by multilayer surfacing. *Russ. Engin. Res.*, 2021, vol. 41, pp. 848-850. https://doi.org/10.3103/S1068798X21090264
12. Kirichek A.V., Solovyov D.L., Zhirkov A.A., Fedonin O.N., Fedonina S.O., Khandozhko A.V. Vozmozhnosti additivno-subtraktivno-uprochnyayushchey tekhnologii [Potentialities in additive-subtractive-strengthening techniques]. *Vestnik BGTU – Bulletin of Bryansk State Technical University*, 2016, no. 4(52), pp. 151-160. https://doi.org/10.12737/23204
13. Fedonina S.O. *Povysheniye kachestva sintezirovannykh iz provoloki detaley volnovym termodeformatsionnym uprochneniyem* [Improving the quality of parts synthesized from wire by wave thermal deformation hardening]. PhD Dissertation, Bryansk State Technical University, Bryansk, 2021. 186 p.
14. Keller I.E., Kazantsev A.V., Dudin D.S., Permyakov G.L., Kartashev M.F. Shape distortions, plastic strains and residual stresses after one-sided forging/rolling of the beam: Application to additive manufacturing of the linear metal segment with layer-by-layer pressure treatment. *Vychisl. mekh. splosh. sred – Computational continuum mechanics*, 2021, vol. 14, no. 4, pp. 434-443. https://doi.org/10.7242/1999-6691/2021.14.4.36
15. Khan A.S., Huang S. *Continuum theory of plasticity*. John Wiley & Sons, 1995. 421 p.
16. LS-DYNA® Keyword user's manual. Volume II. Material models. Ver. R13. LSTC, 2021. 1993 p. http://ftp.lstc.com/anonymous/outgoing/jday/manuals/LS-DYNA_Manual_Volume_II_R13.pdf (accessed 3 February 2022)
17. Nicholas T. Tensile testing of materials at high rates of strain. *Experimental Mechanics*, 1981, vol. 21, pp. 177-185. https://doi.org/10.1007/BF02326644
18. Bragov A.M., Lomunov A.K. Methodological aspects of studying dynamic material properties using the Kolsky method. *Int. J. Impact Eng.*, 1995, vol. 16, pp. 321-330. https://doi.org/10.1016/0734-743X%2895%2993939-G
19. Maker B.N., Zhu X. Input parameters for metal forming simulation using LS-DYNA. 3rd European LS-DYNA Conf. Paris, France, June, 2001. https://www.dynalook.com/conferences/european-conf-2001/58.pdf (accessed 3 February 2022)
20. Trushnikov D.N., Kartashev M.F., Bezukladnikov I.I. Method for controlling surfacing process. RF Patent No. 2750994. Bull. Izobret. 19, 07 July 2021.
21. Rohde J., Jeppsson A. Literature review of heat treatment simulations with respect to phase transformation, residual stresses and distortions. *Scand. J. Metall.*, 2000, vol. 29, pp. 47-62. https://doi.org/10.1034/j.1600-0692.2000.d01-6.x
22. Avrami M. Kinetics of phase change. I. General theory. *J. Chem. Phys.*, 1939, vol. 7, pp. 1103-1112. https://doi.org/10.1063/1.1750380
23. Avrami M. Kinetics of phase change. II. Transformation-time relations for random distribution of nuclei. *J. Chem. Phys.*, 1940, vol. 8, pp. 212-224. https://doi.org/10.1063/1.1750631.
24. Avrami M. Kinetics of phase change. III. Granulation, phase change, and microstructure. *J. Chem. Phys.*, 1941, vol. 9, pp. 177-184. https://doi.org/10.1063/1.1750872

25. Johnson W.A., Mehl R.F. Reaction kinetics in process of nucleation and growth. *Trans. Am. Inst. Min. Met. Eng.*, 1939, vol. 135, pp. 416-442.
26. Sellars C.M. Modelling microstructural development during hot rolling. *Mater. Sci. Technol*., 1980, vol. 6, pp. 1072-1081. https://doi.org/10.1179/MST.1990.6.11.1072
27. Weinberg M., Birnie D.P., Shneidman V.A. Crystallization kinetics and the JMAK equation. *Journal of Non-Crystalline Solids*, 1997, vol. 219, pp. 89-99. https://doi.org/10.1016/S0022-3093(97)00261-5
28. Fernández A.I., Uranga P., López B., Rodriguez-Ibabe J.M. Static recrystallization behaviour of a wide range of austenite grain sizes in microalloyed steels. *ISIJ International*, 2000, vol. 40, pp. 893-901. https://doi.org/10.2355/ISIJINTERNATIONAL.40.893
29. Leblond B., Devaux J. A new kinetic model for anisothermal metallurgical transformations in steels including effect of austenite grain size. *Acta Metall.*, 1984, vol. 32, pp. 137-146. https://doi.org/10.1016/0001-6160(84)90211-6
30. Raghunathan N., Zaidi M.A., Sheppard T. Recrystallization kinetics of Al–Mg alloys AA 5056 and AA 5083 after hot deformation. *Mater. Sci. Tech.*, 1986, vol. 2, pp. 938-945. https://doi.org/10.1179/mst.1986.2.9.938
31. GOST 1497-84. Metals. Methods of tension test. Moscow, Standartinform, 2008. 24 p.

The paper was submitted 25.05.2022; approved after reviewing 19.06.2022; accepted for publication 19.06.2022